MDPI

Article

Differences in Pore Type and Pore Structure between Silurian Longmaxi Marine Shale and Jurassic Dongyuemiao Lacustrine Shale and Their Influence on Shale-Gas Enrichment

Pengwei Wang *[ID], Haikuan Nie, Zhongbao Liu, Chuanxiang Sun, Zhe Cao, Ruyue Wang and Pei Li

Research Institute of Petroleum Exploration & Production, SINOPEC, Beijing 100083, China
* Correspondence: wangpw.syky@sinopec.com

Abstract: The Silurian Longmaxi (S_1l) marine shale and Jurassic Dongyuemiao (J_1d) lacustrine shale in the Sichuan Basin, West China have attracted considerable attention from the oil-and-gas industry in China. Currently, the differences in pore types and pore structures between them are poorly understood, which has limited shale-resource exploration in the Sichuan Basin. This paper systemically compares the pore characteristics of Longmaxi shale and Dongyuemiao shale and investigates their impact on shale-gas enrichment by integrating field-emission scanning electron microscopy (FE–SEM), X-ray diffraction (XRD), low-pressure gas (CO_2 and N_2) adsorption and mercury-intrusion porosimetry, high-pressure sorption isotherms, gas-saturation measurement, molecular-dynamics simulation, etc. The results show that the S_1l organic-rich marine shale and the J_1d lacustrine shale have different pore types and pore structures. The S_1l shale is dominated by organic pores, mainly micropores and mesopores with ink-bottle-like pore shapes, while the J_1d shale is primarily composed of clay-mineral pores, mainly mesopores and macropores with slit- or plate-like pore shapes. Organic pores can provide considerable storage space for shale-gas enrichment in S_1l marine shale, which also determines the adsorption capacity of shale reservoirs. Although organic pores are not the most prevalent in the Dongyuemiao lacustrine shale, they also play an important role in enhancing reservoir quality and absorbed-gas enrichment. Clay-mineral pores contribute weakly to the storage space of J_1d-lacustrine-shale reservoirs. Mesopores are the most important form of storage space in both S_1l shale and J_1d shale, contributing significantly to shale-gas enrichment. Micropores are secondary in importance in S_1l marine shale, while macropores are secondary contributors to pore volume in J_1d lacustrine shale.

Keywords: pore types; pore structure; marine shale; lacustrine shale; Sichuan Basin

1. Introduction

Advanced horizontal drilling and multistage hydraulic fracturing have enabled commercial natural oil and gas to be produced from unconventional shale reservoirs in both North America and China [1,2]. One such unconventional shale-gas system is Silurian Longmaxi organic-rich marine shale, which acts as both a source rock and a reservoir for the Fuling gas field in the Sichuan Basin, West China; it is the first major commercial shale gas to have been discovered outside of North America [3–5]. Currently, industrial shale-gas flow is obtained from the Jurassic Dongyuemiao lacustrine shale in the Sichuan Basin, with a gas flow of 857 m^3/d, exhibiting a promising shale-gas exploration-and-development prospect [6,7]. Although shale-gas resources appear to be regionally pervasive, commercial production or "sweet spots" only occur in high-quality reservoirs with resource potential [8]. Hence, understanding reservoir quality, e.g., petrophysical properties, permeability, pore types, pore geometry, etc., is of great importance in investigating shale-gas mechanisms and guiding shale-gas-exploration activities.

The pore systems, e.g., pore development, geometry, etc., in the Silurian Longmaxi shale and the Jurassic Dongyuemiao lacustrine shale in the Sichuan Basin were widely

investigated in previous studies [9–11]. The factors affecting the development and evolution of micro- and nano-pores can be generally summarized as external and internal. The external factors are mainly the sedimentary environment, structural background, burial depth, temperature, and pressure, while the internal factors include the lithology, mineral composition, TOC content, kerogen type and maturity, etc. [12–15]. The sedimentary environment and tectonic background jointly determine the material sources for micro- and nano-scale pore-system development in shale, and further control pore evolution in shale reservoirs [16]. The paleogeographic pattern, sedimentary environment, and parent rocks exert an obvious influence on shale lithofacies and material composition [17]. The source material of organic matter varied greatly among different sedimentary environments, indicating differences in the primary controlling factors affecting pore types and structures [18,19]. In other words, the pore structures of organic-rich shale systems developed under different sedimentary environments, especially organic pores, are mainly controlled by the material sources. Stable structural–sedimentary environments, with various mineral types and high organic-matter content, laid a solid foundation for the micro- and nano-pore development in shale reservoirs, resulting in the development of different micro- and nano-pore types at various lithofacies, e.g., siliceous shale, calcareous shale, argillaceous shale, etc. [6,15]. Internal factors, such as the lithology, mineral composition, etc., control the pore structures of shale rocks; brittle minerals are conducive to the preservation of primary pores in shale [19–22]. Previous studies showed that the brittle mineral content has a positive correlation with pore volume [10]. Clay-mineral types and content can also exert a significant impact on the pore types and pore volumes of shale reservoirs; the clay minerals in shale have large specific surface areas and high pore volumes [7]. Ji et al. (2012) contended that the specific surface area of montmorillonite was significantly higher than that of illite, chlorite, kaolinite, etc., and the pore structures varied greatly among different clay minerals [23]. The TOC content and kerogen type govern the variation in pore volume and specific surface area associated with organic pores, while the thermal maturation of organic matter restricts the evolution of different pore types [24,25]. Many studies have confirmed that the TOC content contributes greatly to pore development in shale reservoirs, and is mostly positively correlated with pore volume, specific surface area, and porosity. The nano-pore structures of Lower Silurian Longmaxi marine shale in the Sichuan Basin were analyzed, and organic pores were found to contribute greatly to the pore volume and specific surface area [26,27]. Behar and Vandenbroucke (1987) suggested that the organic-pore structure in shale depends on the kerogen type; in their study, the porosity and specific surface area decreased from sapropel-prone mixed-type kerogen to sapropel-type kerogen [28]. The impact of thermal maturation on pore structures is complicated and, currently, controversial, because thermal maturity is a comprehensive reflection of various geological processes.

Moreover, the difference in pore types and pore structures between the Silurian Longmaxi (S_1l) marine shale and the Jurassic Dongyuemiao (J_1d) lacustrine shale in the Sichuan Basin is currently poorly understood, and requires a thorough investigation. This paper systemically compares the pore characteristics of Longmaxi shale and Dongyuemiao shale and investigates their role in shale-gas enrichment through integrating field–emission scanning electron microscopy (FE–SEM), X-ray diffraction (XRD), low-pressure gas (CO_2 and N_2) adsorption and mercury-intrusion porosimetry, high-pressure sorption isotherms, gas-saturation measurement, and molecular-dynamics simulation, etc. The paper provides significant insight into investigations of shale-gas-enrichment mechanisms.

2. Geological Setting

The Sichuan Basin is a petroliferous basin located in the northwest of the Yangtze meta-platform in West China. It is structurally bounded by the Qiyue Mountains in the east, the Daliang Mountains in the south, the Longmen Mountains in the west, and the Daba Mountains in the north (Figure 1a), including several structural units, namely, the Longmenshan–Micangshan structural-complex belt, the Dabashan–Xuefengshan structural-complex belt, the high-and-steep fault-fold zone in South Sichuan, the gentle-fault-fold belt in Central Sichuan, and the gentle-fault-fold belt in West Sichuan. The study area in this paper is situated in the Dabashan–Xuefengshan structural-complex belt, with wide and gentle anticlines confined by some high-angle reverse faults. It has experienced multiple tectonic movements, e.g., Caledonian from the Late Sinian to the Silurian, Hercynian from the Devonian to the Permian, Indosinian during the Triassic, Yanshanian from the Jurassic to the Cretaceous, and Himalayan from the Tertiary to the Quaternary [29–31]. Large-scale tectonic compression and erosion occurred due to uplifts after the late Cretaceous. Most of the Jurassic–Quaternary sequences were eroded by the Yanshanian and Himalayan movement, which was evidenced by thin Jurassic sediments.

The Dabashan–Xuefengshan structural-complex belt was subsequently filled by marine sediments, such ascarbonates, mudstones, and shale, from the Neoproterozoic to the Middle Triassic, and by terrestrial clastic sediments from the Late Triassic to the Paleogene (Figure 1b). The marine sediments vary greatly in thickness, ranging from 3500 m to 6000 m, among which the most extensive and organic-rich shale developed in the Upper Ordovician Wufeng (O_3w) and Lower Silurian Longmaxi (S_1l). During the rapid global sea-level rise during the Late Ordovician and Early Silurian, a deep-water shelf developed in the confined paleogeography of the study area, where a succession of O_3w-S_1l marine organic-rich shale was deposited in low-energy and anoxic sea water [32,33]. Specifically, the shale from the O_3w to the bottom of the S_1l was mainly deposited in the transgressive systems tract, early highstand systems tract, and late highstand systems tract upward [34,35]. The S_1l shale on the top of the O_3w shale is mainly composed of black siliceous shale, carbonaceous shale, and argillaceous siltstone [30–32].

The Jurassic system is well developed and widely distributed in the Sichuan Basin. The Lower Jurassic Ziliujing Formation, which includes Zhenzhuchong Member, Dongyuemiao Member, Maanshan Member, and Da'anzhai Member from bottom to top, is about 300–400 m in thickness. Two lacustrine shales, Dongyuemiao shale and Da'anzhai shale, were deposited at shallow and semi-deep lake depths as responses to the subsidence and lake transgression of different scales. Lake transgression occurred during the Zhenzhuchong–Dongyuemiao period, with the maximum transgression occurring during the Dongyuemiao period [7,33]. The Dongyuemiao Member is dominated by black shale, brownish-gray limestone, and siltstone, whose thickness is >150 m at the center and is 20 m at the margin [33,34]. Small-scale lake regression occurred from the Dongyuemiao period to the Ma'anshan period; as a result, shallow-lake deposits can be found at most of the deposition centers.
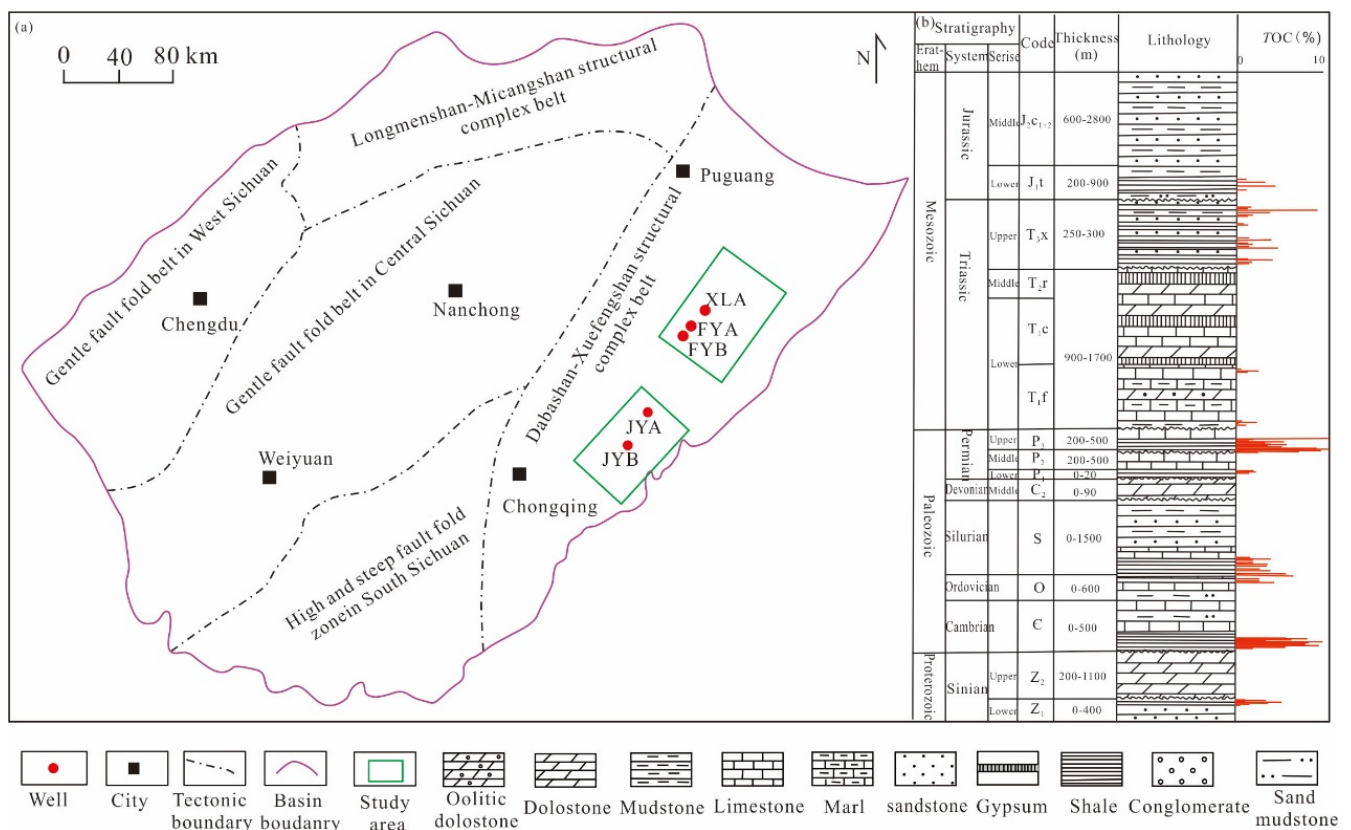
Figure 1. Structural units (**a**) and generalized stratigraphic column (**b**) of the Sichuan Basin, West China; (**b**) was modified from [35].

3. Samples and Methods

3.1. Samples

A total of 49 samples were collected from 5 wells (see locations at Figure 1a) to investigate control of pore types and pore structures over shale-gas enrichment. In total, 19 S_1l marine shale samples were obtained from JYA well and JYB well, including siliceous shale and argillaceous shale, while 24 J_1d lacustrine shale samples, primarily argillaceous shale, were collected from XL A well, FY A well, and FY B well.

3.2. Methods

Shale samples were crushed and sieved into grains of 80–100 mesh powder for total organic carbon (TOC, wt%) measurement and X-ray diffraction (XRD). Before the TOC measurement, powdered shale samples were treated with hydrochloric acid to remove carbonate and were washed with distilled water 2 h later. Next, powders were dried overnight at 70 °C. Subsequently, the measurement was performed on a LECO CS-200 carbon/sulfur analyzer. Bulk mineralogical composition analysis of randomly oriented shale powders were carried out on a D8 Discover X-ray diffractometer. The working voltage and current were 40 kV and 40 mA, respectively. Samples were crushed and powdered in ethanol for 15 min to reduce the water-soluble mineral dissolution, form uniform crystallite sizes, and prevent excess strain and heat damage. Mineral content was calculated based on diffraction patterns and RIR method.

Field emission–scanning electron microscopy (FE–SEM) was performed on shale samples with an FEI Quanta 250 field emission–scanning electron microscope. These samples were cut and polished using an Ar–ion milling instrument to produce a smooth surface with minor topographical variation. Secondary electron (SE) images were used to record topographical variation, while backscattered electron (BSE) images were employed to show composition variation at working distance of 2.7 mm and voltage of 1.5 kV.

Low-pressure gas adsorption and mercury-intrusion porosimetry were conducted to describe the pore structure in shale system. The low-pressure gas adsorption was performed to describe micropores and mesopores using a Quantachrome® Autosorb-iQ2-MP apparatus and a Micromeritics ASAP 2020 Surface Area and Porosity Analyzer, respectively. Samples were crushed and sieved to 60–80 mesh size, after which they were dried in an oven at 110 °C for 4 h and degassed in a vacuum at 80 °C for 24 h. The CO_2 sorption was determined at pressure of 4×10^4–3.2×10^2 Pa and temperature of 0 °C [36]. A variety of theoretical digital models (BET, BJH, QSDFT, and HK) were employed to calculate available pore volume, pore size, and specific surface area. The N_2 adsorption isotherms were simulated at temperature of −196.15 °C under a P/Po of 0.005–0.99 [36]. Surface area was quantitatively determined based on the BET equation [37]. Pore volume and pore size were calculated based on the Barrett, Johner, and Halenda (BJH) method. Average pore diameters were determined with the ratio of the total-adsorbed-nitrogen amount to the available surface area under the assumption of cylindrical pore geometry. Crashed and dried samples were infused with mercury on a Micromeritics™ Autopore IV 9500-series apparatus from 0.004 MPa to 144.1308 MPa.

High-pressure-sorption isotherms were measured on an Isothermal Adsorption Analyzer ISO-200 with ultra-high purity (99.99%) methane as the adsorbate. This was performed at a consistent temperature of 30 °C and a pressure of up to 12 MPa. In total, 24 dry samples were crushed and sieved to powders with sizes of less than 60 mesh to reduce the influence of grain size and moisture on the sorption capacity. Before the measurements were conducted, the samples were dried in a vacuum oven for 24 h at 105 °C to remove moisture. The Langmuir expression, describing the variation in adsorption capacity with temperature and pressure, was employed to parameterize adsorption behaviors [38,39].

Gas saturations were calculated through moisture-equilibrating the samples at room temperature of 24 °C. Samples (10 g) were crushed into grains with particle sizes of 0.5–1.0 mm. Subsequently, they were dried at 110 °C to determine their dry weights (M_d). Finally, they were equilibrated in an evacuated desiccator until reaching weight constancy (M_w). The water saturation (S_w) was determined using Equation (1). Next, gas saturation was calculated by excluding the measured water saturation from 100%.

$$S_w = \frac{M_w - M_d}{M_d} \times 100\% \qquad (1)$$

A molecular-dynamics simulation was performed to simulate methane adsorption at pores associated with illite using Materials Studio to determine impact of water saturation on adsorption capacity of clay minerals [40,41]. The assumed temperature of 63 °C and pressure of 31.34 MPa were derived from Dongyuemiao lacustrine shale from the FY A well, whose methane density was 0.185 g/cm³. The force field simulated was COMPASSII type; charge was assigned by the force field. The cut-off radius of Van Der Waals force was assumed as 1.25 nm. Pores were designed with slit-like shapes based on SEM observation, with lengths of 10 nm. The total methane-adsorption amount and free-methane volume were simulated to determine the excess adsorption amount. Total adsorption amount was defined as the total gas amount in pore space under particular temperature and pressure, including free gas in the available pore space and adsorbed gas on pore surface. Excess adsorption amount was the difference between the adsorbed gas amount at porous volume and the adsorbed gas amount at the same volume without pore wall, namely, excess adsorption amount = total adsorption amount − free volume × bulk phase density.

4. Results

4.1. TOC and Mineral Components

The measurement suggested that the two shale types differ in their TOC (Figure 2). This was in a range of 1.08%–6.39% for the Silurian Longmaxi marine-shale samples, with an average value of 3.47%, while it was 0.48%–2.10% for the Lower Jurassic Dongyuemiao lacustrine-shale samples, averaging 1.25%. The bulk-mineralogical-composition analysis showed that both the Silurian Longmaxi marine shale and the Dongyuemiao lacustrine shale are composed of quartz, feldspar, clay minerals, carbonate, pyrite, etc. (Figure 3). The Longmaxi marine shale is rich in quartz and feldspar compared with the Dongyuemiao lacustrine shale, with average contents of quartz and feldspar of 52.22%, followed by clay minerals, with contents of 33.05%. However, the Dongyuemiao lacustrine shale samples had high clay-mineral contents, with an average value of 65.49%; the quartz and feldspar contents were only 32.41%.
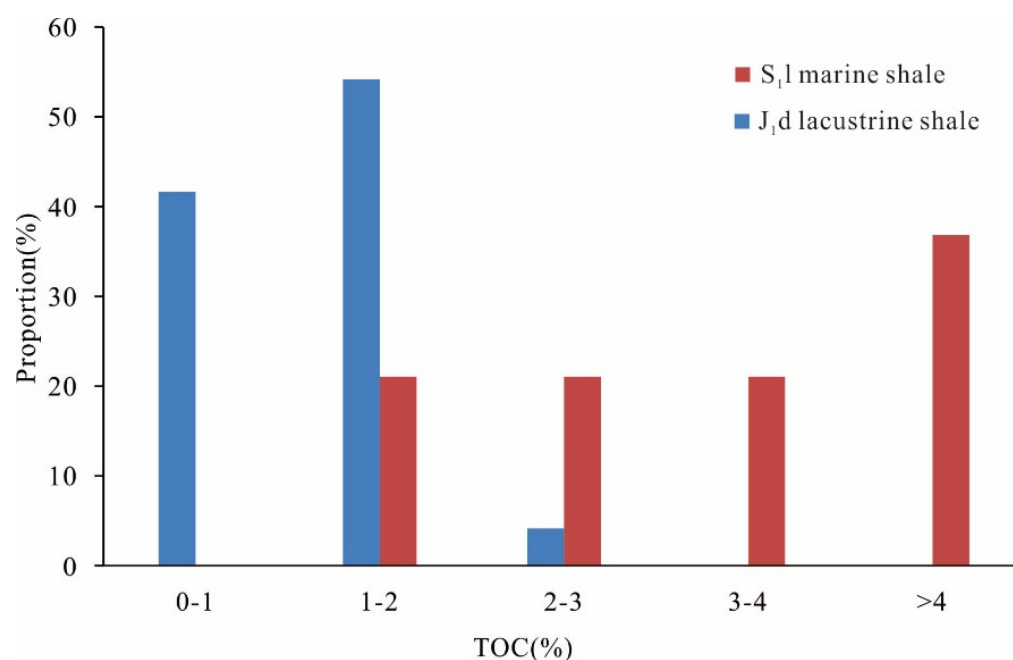

Figure 2. Histogram showing the measured TOC of the Silurian Longmaxi marine-shale samples and the Lower Jurassic Dongyuemiao lacustrine-shale samples.

4.2. Pore Types

The petrologic observations from the SEM images suggested that the pore system in the S_1l organic-rich marine shale is dominated by organic pores (OM pores). Residual intergranular pores and intragranular dissolved pores were found in the S_1l shale; these were frequently filled by bitumen (Figure 4). The organic pores were uniformly distributed in the bitumen-filling pore space between inorganic grains. The bitumen observed has no typical scale or shape, which are greatly determined by inorganic pores. A previous study [20] suggested that, in addition to bitumen, organic pores in S_1l shale were also well developed in kerogen, depending on the maceral; abundant spongy organic pores grew well in camulticellular algae and were poorly developed in unicellular algae. Organic pores vary randomly in pore shape; they are commonly ellipse-like, subrounded, rounded, subangular, or irregular in shape. Significant differences in pore size can be observed in the SEM images, in which the pores in the center of bitumen are generally larger than those at the edge (Figure 4a–c). Some of the organic pores observed bent at the edges of the inorganic minerals (Figure 4b) or were obviously oriented along the extension of the bitumen (Figure 4a,c), indicating the negative impact of mechanical compaction on organic-pore preservation. However, the organic pores in some of the samples had no

obvious major axis or minor axis; these pores might have been well protected from being collapsed by intensive mechanical compaction by frameworks derived from inorganic minerals. Furthermore, oil cracking into gas can increase the pressure in shale reservoirs significantly; this often generates overpressure, which can help to prevent these pores from being deformed or destroyed, which contributes greatly to organic-pore preservation in S_1l shale reservoirs [31,42,43].
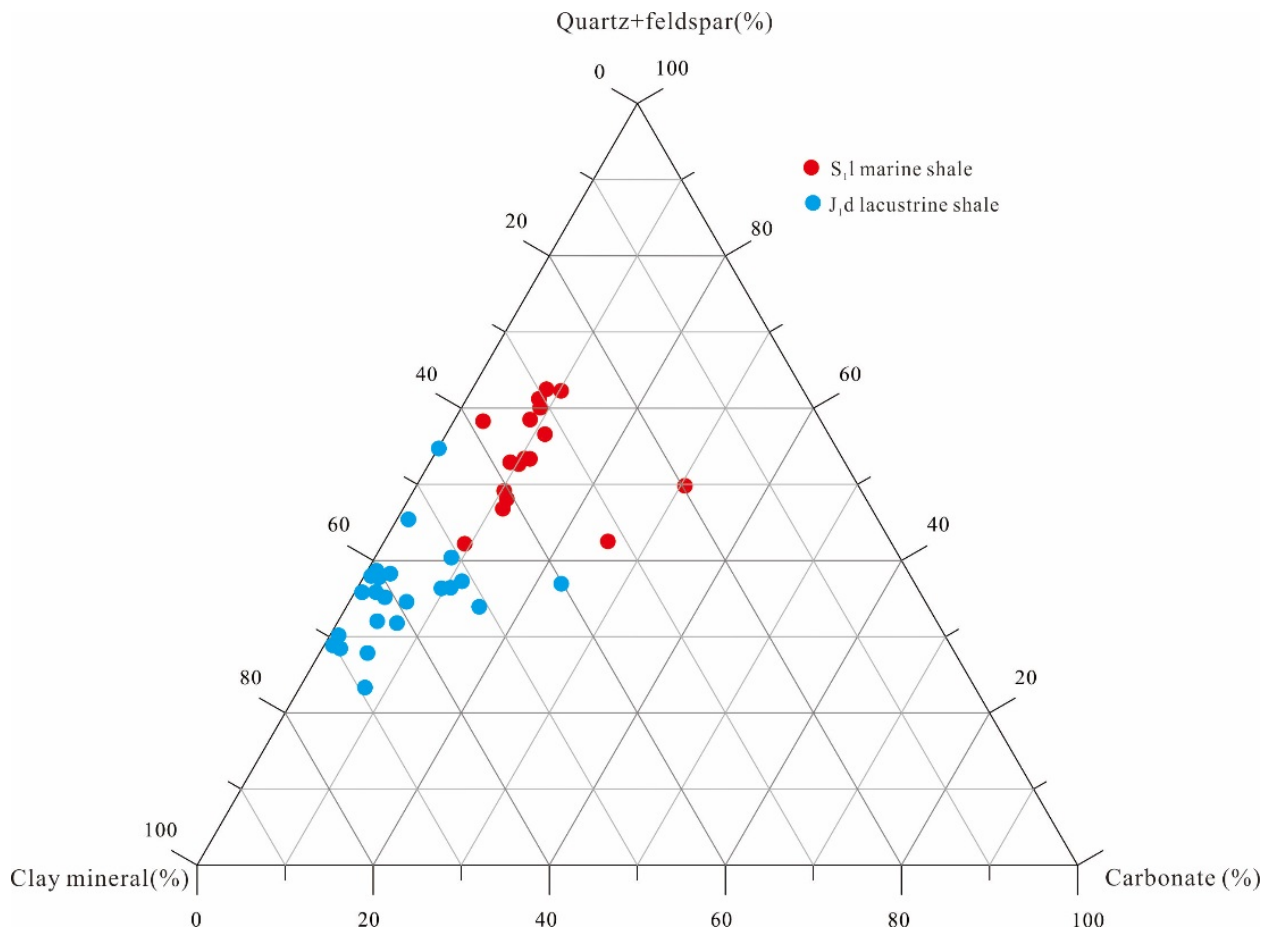

Figure 3. Triangle diagram of mineral components of the Silurian Longmaxi marine-shale samples and the Lower Jurassic Dongyuemiao lacustrine-shale samples.

Unlike the S_1l organic-rich marine shale, the J_1d lacustrine shale was dominated by clay mineral pores (CL pores), followed by organic pores (Figure 5a). The clay minerals observed in the SEM images, mainly illite/smectite mixed layers and illite, with only a small group of chlorite and kaolinite [7], were commonly directionally arranged with slip-sheet structures (Figure 5a,b). Considerable nano-scale or micro-scale pores appeared between or within the well-orientated clay minerals. These clay-mineral-hosted pores differed in shape; they were mostly slit- or plate-like, strip-like, triangular, and irregular in shape, with rough surfaces. They were also inhomogeneous in size; the maximum diameter was several hundreds of nanometers (Figure 5b). These pores were typically derived from the phase transition and dehydration of clay minerals that experienced intensive compaction with increasing overburden. This was confirmed by the obvious convergence of the clay minerals, e.g., slit-like illite, whereas the pores associated with plate-like clay mineral interlayers were well preserved and supported by pyrite grains (Figure 5a). Importantly, these pores were completely or partly filled by bitumen or primary organic matter (Figure 5a–c). These organic matters had no fixed shape, varying greatly as a function of the clay-mineral-hosted pore shape. This was a good indication that they may have been the migrated organic

matter, such as pyrobitumen originating in kerogen thermal degradation [44]. The organic pores were heterogeneously developed in bitumen, mostly in honeycomb-like, elliptical, round and irregular shapes. However, no obvious organic-pore growth was found in some of the organic matter; several bubble-like pores were found at the margin, but these were small (Figure 5c). They were typically vitrinite distributed as belts or blocks with uniform surfaces, which are associated with the humification and gelification of woody fibers from higher plants (Figure 5c,d) [45,46]. The pores in the vitrinite were commonly inherited from original cell structures, rather than developing in relation to thermal maturation. However, gas-generation processes can shrink vitrinite to produce pores or microfractures between vitrinite and inorganic minerals; in such cases, brittle minerals, such as pyrites, can help pores to become effective storage spaces.
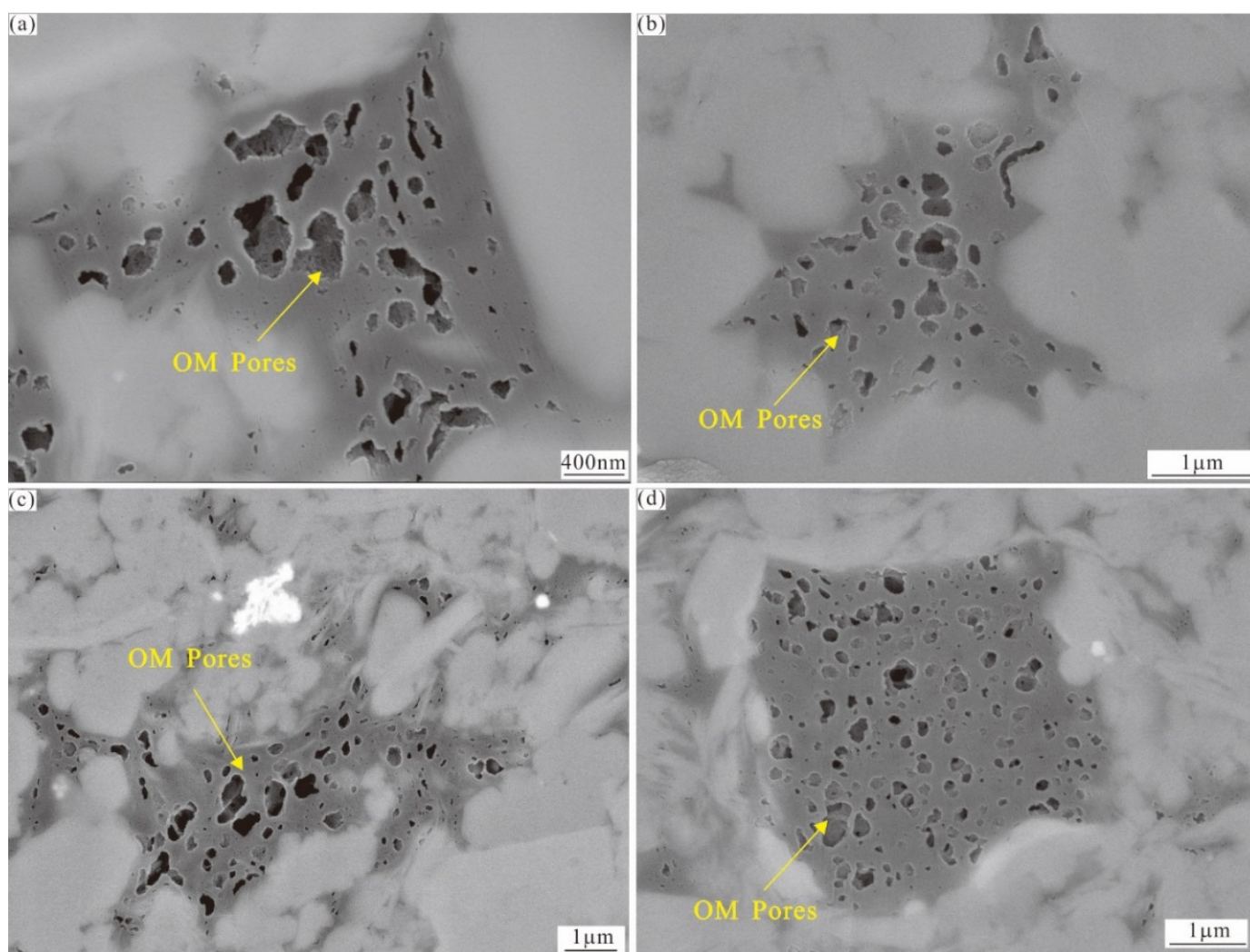

Figure 4. SEM images showing pore types of the Silurian Longmaxi marine shale. (**a**) Gray–black siliceous shale, TOC = 3.69%; (**b**) gray–black carbonaceous shale, TOC = 3.29%; (**c**) gray–black carbonaceous shale, TOC = 2.94%; (**d**) gray–black siliceous shale, TOC = 3.81%.
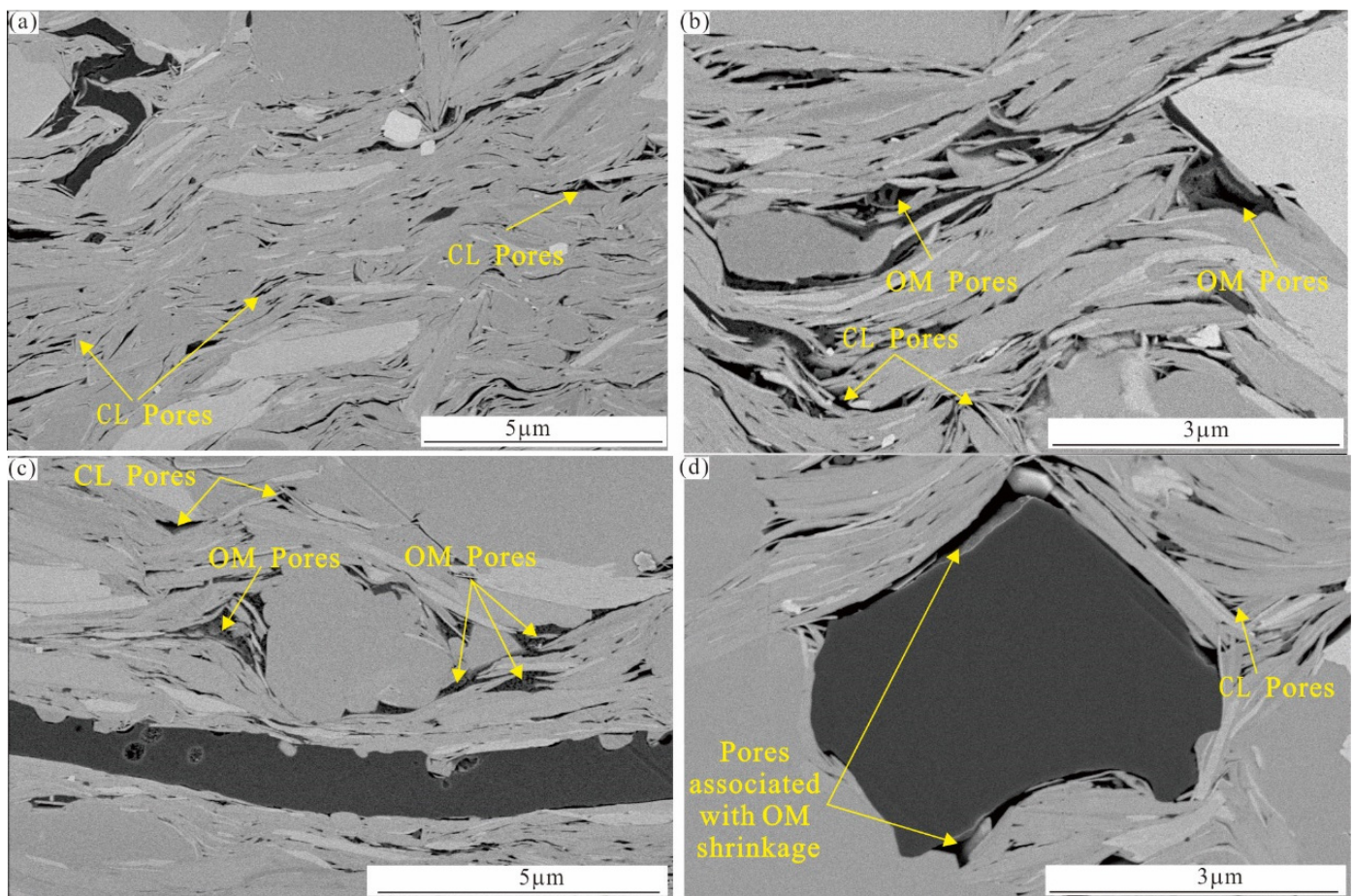
Figure 5. SEM images showing pore types of the Lower Jurassic Dongyuemiao lacustrine shale. (**a**) FY B well, gray argillaceous shale, TOC = 1.33%; (**b**) XL A well, gray argillaceous shale, TOC = 1.96%; (**c**) FY B well, gray argillaceous shale, TOC = 1.64%; (**d**) XL A well, gray argillaceous shale, TOC = 1.46%.

4.3. Pore Sizes

The combined low-pressure gas-adsorption measurement and high-pressure mercury-intrusion porosimetry suggested that the pore system in the Silurian Longmaxi marine shale dominated by organic pores was mainly composed of micropores (<2 nm), followed by mesopores (2–50 nm) (Figure 6a), according to the pore-size classifications from the International Union of Pure and Applied Chemistry (IUPAC) [47]. Unlike the Silurian Longmaxi marine shale, the Dongyuemiao lacustrine shale was mainly composed of mesopores, with macropores of secondary importance, with the micropores only making up a small proportion. This can be attributed to the differences in pore type between the marine shale and the lacustrine shale. As Figure 4 shows, organic pores were prevalent in the Silurian Longmaxi marine shale; these were small in size, commonly less than hundreds of nanometers. However, clay-mineral pores were popular in the Dongyuemiao lacustrine shale, and they were significantly larger than the organic pores. Furthermore, fracture occurrence associated with clay minerals and organic matter (Figure 5b,d) contributed greatly to the macropores in the Dongyuemiao lacustrine shale, in which a small group of micropores were classed as organic. Previous studies confirmed that the size of organic pores varies significantly with the thermal maturation of source rocks; pore size follows an increasing trend with thermal maturity at a vitrinite reflectance (R_o) of 1.2%–2.0% (at the stage of early oil cracking into wet gas), after which it exhibits a decreasing trend with increasing R_o and, finally, micropores are predominant at a R_o of 2.7% [34,45,48]. The measured R_o was about 2.2%–2.5% in the Silurian Longmaxi marine shale, and it was

about 1.38%–1.58% in the Dongyuemiao lacustrine shale. Therefore, organic pores in the Longmaxi marine shale were smaller than those in the Dongyuemiao lacustrine shale, which experienced similar geological events and tectonic activities.
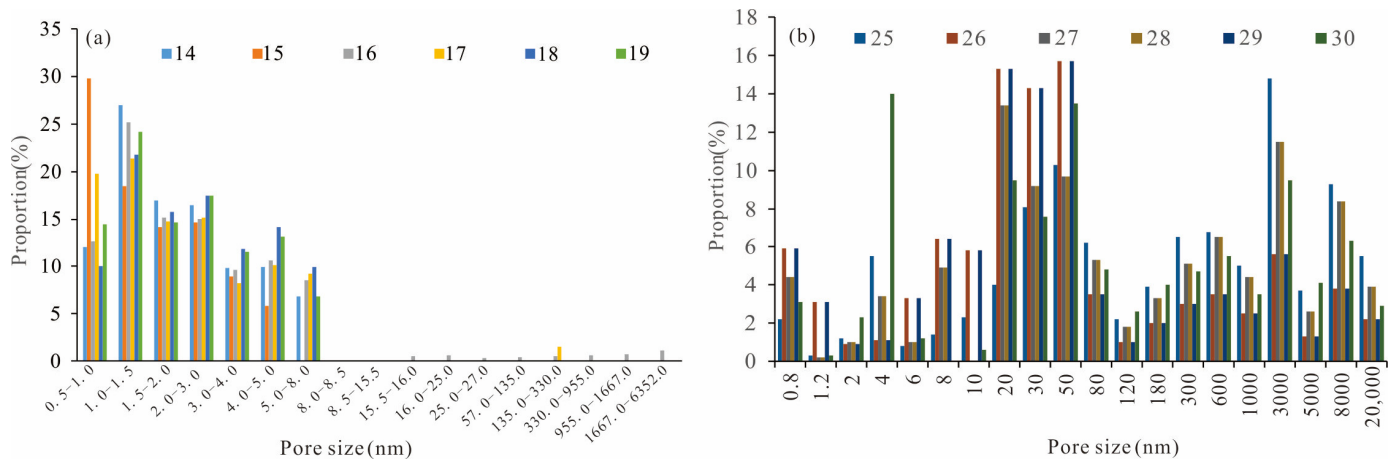

Figure 6. Pore sizes of the Silurian Longmaxi marine-shale samples (**a**) and the Lower Jurassic Dongyuemiao lacustrine-shale samples (**b**).

4.4. Pore Shapes

The Silurian Longmaxi marine-shale samples and the Lower Jurassic Dongyuemiao lacustrine-shale samples had similar nitrogen-adsorption and -desorption isotherms. The isotherm curves were characterized by reversibility at low relative pressure and hysteresis loops at higher relative pressure (relative pressure > 0.5) (Figure 7). The hysteresis loop is mainly generated by capillary condensation, which is a good indicator of mesopore morphology [49,50]. Unique hysteresis loops were found in both the Longmaxi shale and the Dongyuemiao shale samples; they therefore differed from the typical loop established by the International Union of Pure and Applied Chemistry (IUPAC) classification. The pore shapes of the Longmaxi shale samples were similar to the H2 type but also shared some features with the H3 type, indicating an ink-bottle-like pore system dominated by organic pores, with inorganic pores, such as clay-mineral pores, of secondary importance. This phenomenon agrees well with the SEM observations in Figure 4. Unlike the Longmaxi marine shale, the adsorption curves of the Dongyuemiao shale increased sharply when the relative pressure was higher than 0.8. This suggested a slit- or plate-like pore system with a small proportion of ink-bottle-shaped pores, a complex pore geometry jointly controlled by both clay-mineral and organic-matter filling. The total pore volume of the Silurian Longmaxi marine shale was in a range of 0.008–0.1 mL/g; it was lower in the Lower Jurassic Dongyuemiao lacustrine shale, where it ranged from 0.007 mL/g to 0.027 mL/g. Furthermore, the surface area was greater in the Silurian Longmaxi marine shale than in the Lower Jurassic Dongyuemiao lacustrine shale. The values were 7.22–20.38 m^2/g and 2.89–12.14 m^2/g, respectively.

The measurement also showed some differences in pore structure between the two shale types (Table 1). The measured pore volume of the Silurian Longmaxi marine-shale samples was in the range of 0.008–0.366 mL/g, with an average value of 0.018 mL/g, while the values of the Lower Jurassic Dongyuemiao lacustrine -shale samples were between 0.007 mL/g and 0.027 mL/g, averaging 0.016 mL/g. Hence, the Longmaxi marine-shale samples and Dongyuemiao lacustrine-shale samples had no significant differences in pore volume. The specific surface areas of the Silurian Longmaxi marine-shale samples ranged from 7.223 m^2/g to 20.383 m^2/g, with an average of 11.517 m^2/g. However, the Dongyuemiao lacustrine-shale samples were low in specific surface area, varying between 2.898 m^2/g and 12.144 m^2/g, with an average value of 6.780 m^2/g. They were also different in Langmuir volume, represented by VL. Specifically, the VL of the Longmaxi marine-shale

samples was 1.72–6.89 m³/t, averaging 3.26 m³/t, while the range of the Dongyuemiao lacustrine-shale samples was 0.67–1.25 m³/t, with an average of 1.13 m³/t.
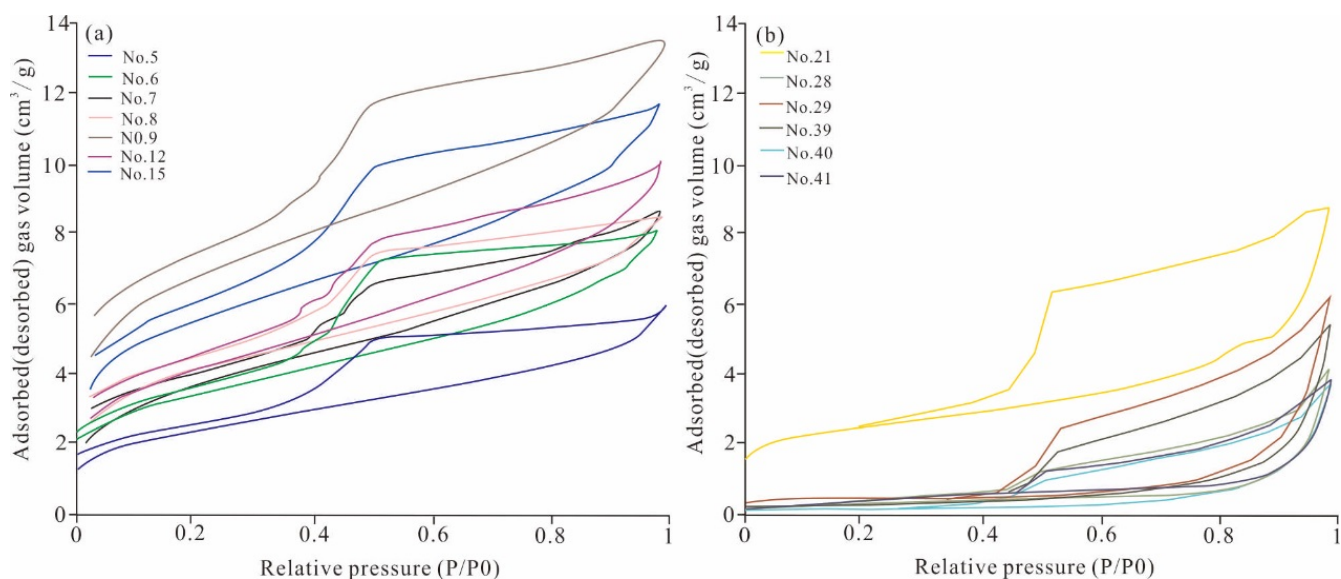

Figure 7. Pore shapes of the Silurian Longmaxi marine-shale samples (**a**) and the Lower Jurassic Dongyuemiao lacustrine-shale samples (**b**).

Table 1. Parameters of pore structures of the Silurian Longmaxi marine-shale samples (a) and the Lower Jurassic Dongyuemiao lacustrine-shale samples from the Sichuan Basin.

Sample No.	Well	Lithology	Pore Volume (mL/g)	Specific Surface Area (m²/g)	VL (m³/t)
1	JYA	Gray–black siliceous shale	0.008	7.22	2.11
2	JYA	Gray–black siliceous shale	0.100	10.22	/
3	JYA	Gray–black siliceous shale	0.008	7.95	1.72
4	JYA	Gray–black siliceous shale	0.009	7.53	2.56
5	JYB	Gray–black argillaceous shale	0.012	11.82	2.34
6	JYB	Gray–black siliceous shale	0.012	10.34	2.22
7	JYB	Gray–black argillaceous shale	0.017	13.58	2.69
8	JYB	Gray–black argillaceous shale	0.008	7.53	3.52
9	JYB	Gray–black argillaceous shale	0.010	9.01	/
10	JYB	Gray–black argillaceous shale	0.013	12.97	/
11	JYB	Gray–black siliceous shale	0.014	12.80	/
12	JYB	Gray–black argillaceous shale	0.012	10.57	4.66
13	JYB	Gray–black siliceous shale	0.011	9.61	4.00
14	JYB	Gray–black siliceous shale	0.013	10.94	/
15	JYB	Gray–black siliceous shale	0.01	9.62	/
16	JYB	Gray–black siliceous shale	0.017	11.71	3.64
17	JYB	Gray–black siliceous shale	0.019	15.45	2.76
18	JYB	Gray–black siliceous shale	0.019	19.59	6.89
19	JYB	Gray–black argillaceous shale	0.024	20.38	/
20	FYA	Gray argillaceous shale	0.019	10.09	0.67
21	FYA	Gray argillaceous shale	0.021	11.00	/
22	FYA	Gray argillaceous shale	0.013	6.47	/
23	FYA	Gray argillaceous shale	0.016	7.59	/
24	FYA	Gray argillaceous shale	0.017	9.50	/
25	FYA	Gray argillaceous shale	0.021	12.14	/

Table 1. *Cont.*

Sample No.	Well	Lithology	Pore Volume (mL/g)	Specific Surface Area (m²/g)	VL (m³/t)
26	FYA	Gray argillaceous shale	0.017	7.57	/
27	FYA	Gray argillaceous shale	0.019	7.46	/
28	FYA	Gray argillaceous shale	0.021	9.69	/
29	FYA	Gray argillaceous shale	0.017	5.52	0.86
30	FYA	Gray argillaceous shale	0.007	2.90	/
31	FYA	Gray argillaceous shale	0.010	2.929	/
32	FYA	Gray argillaceous shale	0.017	7.01	1.00
33	FYA	Gray argillaceous shale	0.027	9.64	/
34	FYA	Gray argillaceous shale	0.015	4.41	1.66
35	FYA	Gray argillaceous shale	0.022	8.01	/
36	XLA	Gray argillaceous shale	0.016	6.20	1.31
37	XLA	Gray argillaceous shale	0.015	9.66	/
38	FYB	Gray siliceous shale	0.018	3.60	0.99
39	FYB	Gray siliceous shale	0.0190	5.92	0.68
40	FYB	Gray siliceous shale	0.015	5.66	/
41	FYB	Gray siliceous shale	0.015	5.69	1.47
42	XLA	Gray argillaceous shale	0.013	4.92	2.15
43	XLA	Gray argillaceous shale	0.013	4.55	1.75
44	XLA	Gray argillaceous shale	0.013	5.03	0.68
45	XLA	Gray argillaceous shale	0.012	4.10	0.71
46	XLA	Gray argillaceous shale	0.012	5.82	0.81

Note: "/" represents no data. VL represents Langmuir volume.

5. Discussion

5.1. Effect of Pore Types on Shale-Gas Enrichment

The plot of the TOC values vs. the measured gas saturation from the Longmaxi marine shale shows a positive correlation (Figure 8a). This is a good indication that well-developed organic pores, as the primary pore type in marine shale, can provide significant storage space for shale-gas enrichment, since it was confirmed that the organic pores in kerogen and bitumen were the primary sites of gas accumulation in shale reservoirs [5,22,34]. Furthermore, high TOC content suggests high gas-generation potential in source rocks, which can provide a solid foundation for gas enrichment in shale reservoirs. Organic-matter abundance is one of the main factors affecting the gas-adsorption capacity (represented by Langmuir volume) of shale reservoirs, contributing positively to the Langmuir volume (Figure 8b). Previous studies [36,51] on the Jurassic Gordondale Formation in northeastern Canada and Mississippian Barnett shale suggest that calcareous shale and siliceous shale with high TOC have a high storage capacity for adsorbed gas. This is because the microp-ores that develop in kerogen or bitumen with oil-wetting surfaces can provide abundant adsorption sites for gaseous hydrocarbons, enhancing adsorption capacity significantly. Unlike organic matter, clay-mineral content is negatively correlated with measured gas saturation, indicating that clay-mineral pores contribute negatively to shale-gas enrich-ment (Figure 8c). Firstly, the contribution to storage space of clay-mineral pores, which accounted for a small proportion of the total pore volume in the Longmaxi marine shale, is minor. Secondly, some clay minerals are water-swelling, which means that they can only supply limited sorption sites under high water saturation [52]. This is evidenced the lack of an obvious correlation between the clay minerals and the Langmuir volume (Figure 8d), indicating that the clay-mineral pores in the Longmaxi marine shale made only a minor contribution to the adsorption capacity. It was confirmed by a previous study by Li et al. (2016) [53] that the adsorption capacity of clay minerals can be significantly reduced by the coexistence of clay minerals, gas, and water, For example, the adsorption capacity of clay minerals in Wufeng–Longmaxi shale at a water saturation of 20%–40% is only 10%–20% of that under dry conditions.
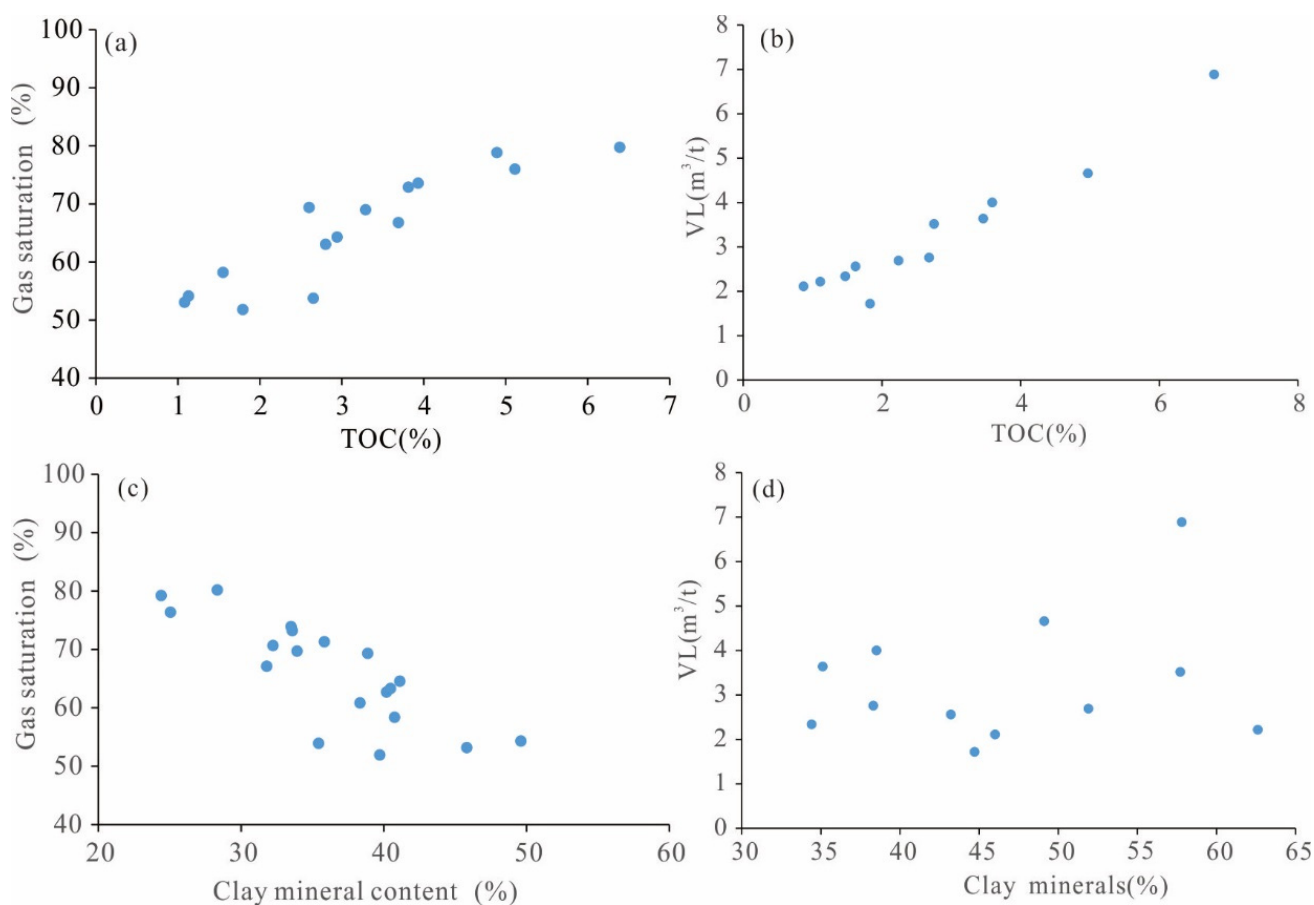
Figure 8. Effect of organic pores (**a**,**b**) and clay-mineral pores on gas content and adsorption capacity (**c**,**d**) in the Silurian Longmaxi marine-shale samples.

Similar to the Silurian marine shale, the organic pores in the Dongyuemiao lacustrine shale had a positive correlation with the gas saturation, indicating that the organic pores in the lacustrine shale also play an important role in enhancing reservoir quality (Figure 9a). Therefore, the low TOC content and low organic pore volume may be partly responsible for the low gas saturation in the lacustrine shale. A positive correlation was observed between the organic pores and the VL, since these nano-scale pores have high specific surface areas, which can provide a high number of sorption sites and improve sorption capacity [36,47]. Unlike the marine shale, which is dominated by type I and type II$_1$ kerogen, the lacustrine shale is generally composed of type II$_1$ and type III kerogen [37]. The Green River shale (type I), Devonian Woodford shale (type II), and Late Cretaceous coal rock (type III) were selected to investigate the adsorption capacities of three organic types [54]. It was suggested that their adsorption capacities were in the following order: type III > type II > type I. This was because the higher number of aromatic structures in the type III kerogen contributed greatly to its stronger adsorption capacity. Hence, it is presumed that the organic matter in the Dongyuemiao lacustrine shale has a higher adsorption capacity than the Longmaxi marine shale under the same geological conditions. Similar to the Longmaxi marine shale, the Dongyuemiao lacustrine shale has a weak correlation between its clay-mineral content and measured gas saturation, which means that clay minerals make a weak contribution to its storage space. This can partly explain why the clay-mineral-rich Dongyuemiao lacustrine shale is low in gas saturation compared with the Silurian marine shale. Furthermore, compared with organic matter, the clay minerals have a positive but weak correlation with the VL (Figure 9d). This was explained by a previous study by Lu et al. (1995) [55], in which it was found that clay minerals, especially illite, can enhance the adsorption behavior of shale samples with low organic carbon. Dongyuemiao

lacustrine shale is low in TOC content (averaging of 1.25%), but high in clay minerals, especially illite/smectite mixed layers and illite, which can make a certain contribution to its adsorption capacity.
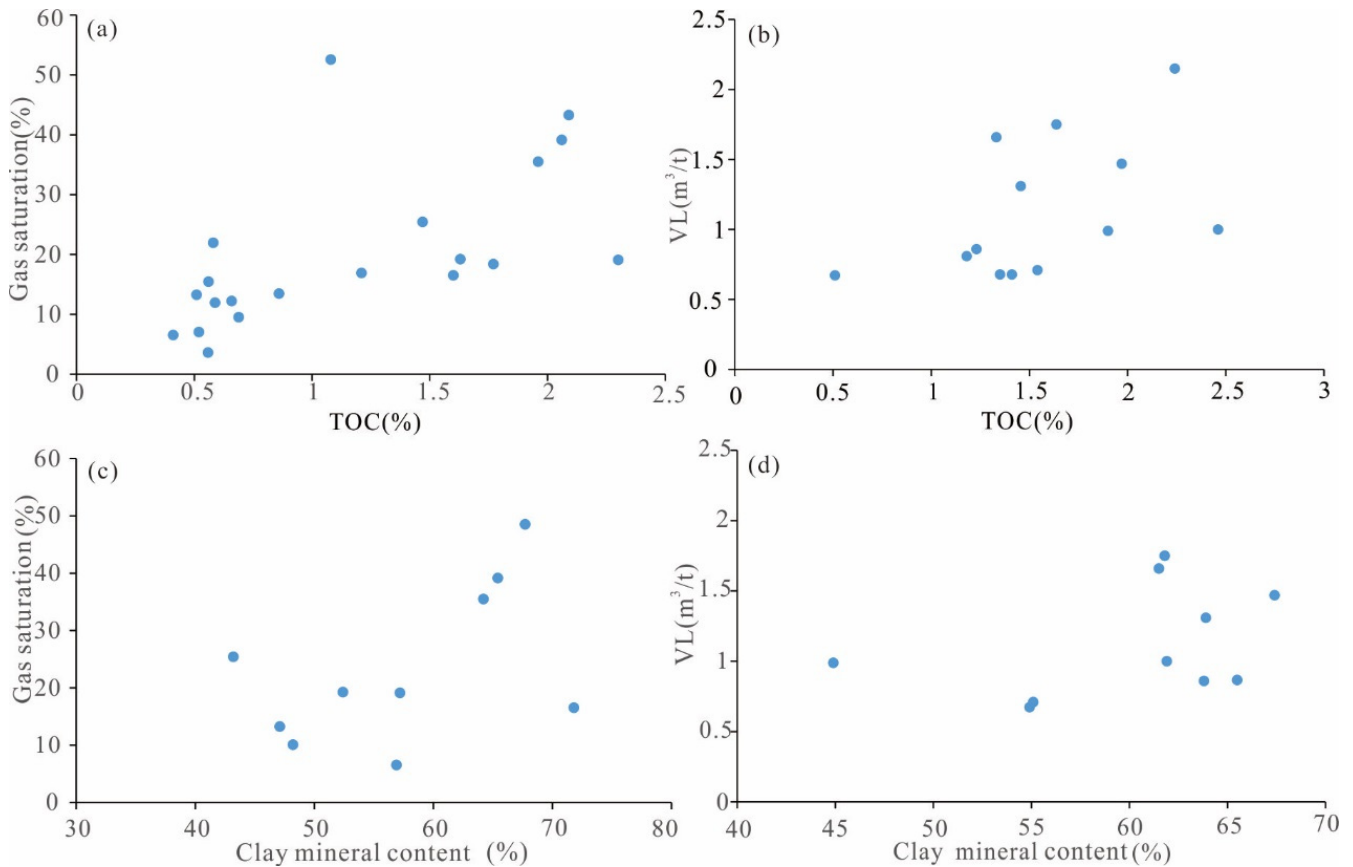

Figure 9. Effects of organic pores (**a**,**b**) and clay-mineral pores on gas saturation and adsorption capacity (**c**,**d**) in the Dongyuemiao lacustrine-shale samples. The VL represents Langmuir volume.

However, as mentioned above, the water in clay mineral pores has a negative effect on the adsorption capacity. The molecular-dynamics simulation suggested that the gas density in illite surfaces decreases significantly when the water saturation increases from 0 to 90% (Figure 10). The simulated adsorbed gas accounts for 31.82% at a water saturation of 0, and it is only 19.31% at a water saturation of 90%, which is a decreased of 39.32%. This suggests that adsorption behavior mainly occurred between illite and gas when the water saturation is low, and that it mainly occurs between water film and gas when the water saturation is high. The measured water saturation in the Dongyuemiao lacustrine shale samples was between 40% and 90%, indicating the minor contribution of the clay minerals to the adsorption capacity.
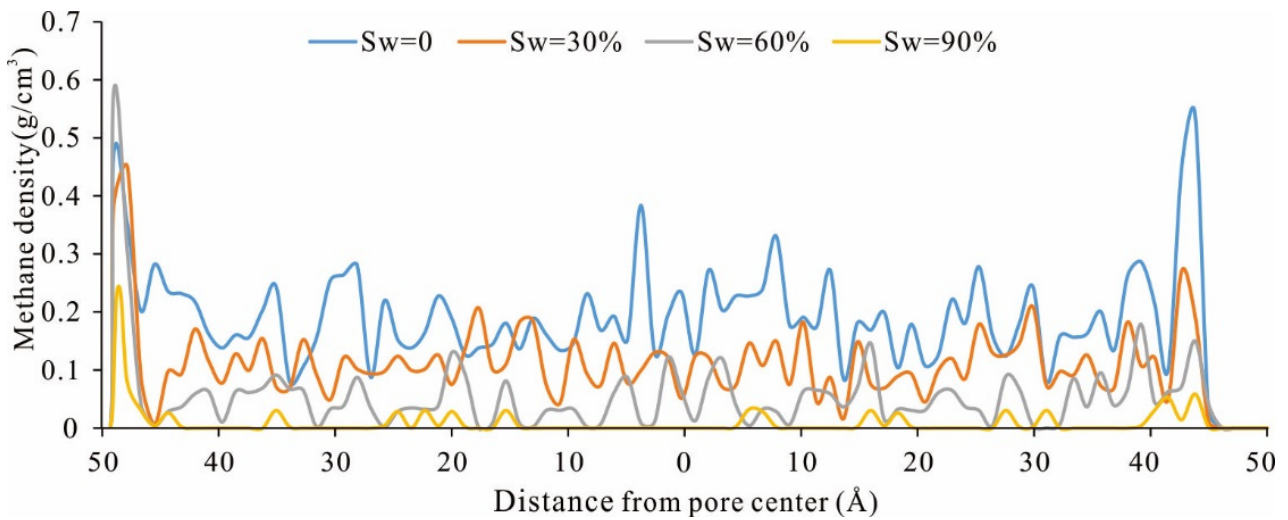
Figure 10. Modeled methane density in nano-scale clay-mineral pores under different levels of water saturation.

5.2. Effect of Pore Sizes on Shale-Gas Enrichment

The comparison between the pore volume and measured gas content in the Silurian Longmaxi marine shale suggested that mesopores provide the highest storage volume in shale reservoirs (Figure 11). Although micropores are large in number, their contribution to storage space is of secondary importance. Macropores supply limited space for shale-gas enrichment. Similar to the Silurian Longmaxi marine shale, the mesopores in the Dongyuemiao lacustrine-shale samples determine the shale-reservoir quality. However, unlike the Longmaxi shale, both the macropores and the micropores in the Dongyuemiao lacustrine shale can provide the shale reservoirs with a certain pore volume. A previous study [40] confirmed that the adsorption energy on the particle surface is the highest, decreasing with as the distance between the gas and the particle surface increases. The adsorption energy is extremely high in pores with diameters <2 nm. Therefore, natural the gas in the micropores mainly occurs as adsorbed gas.
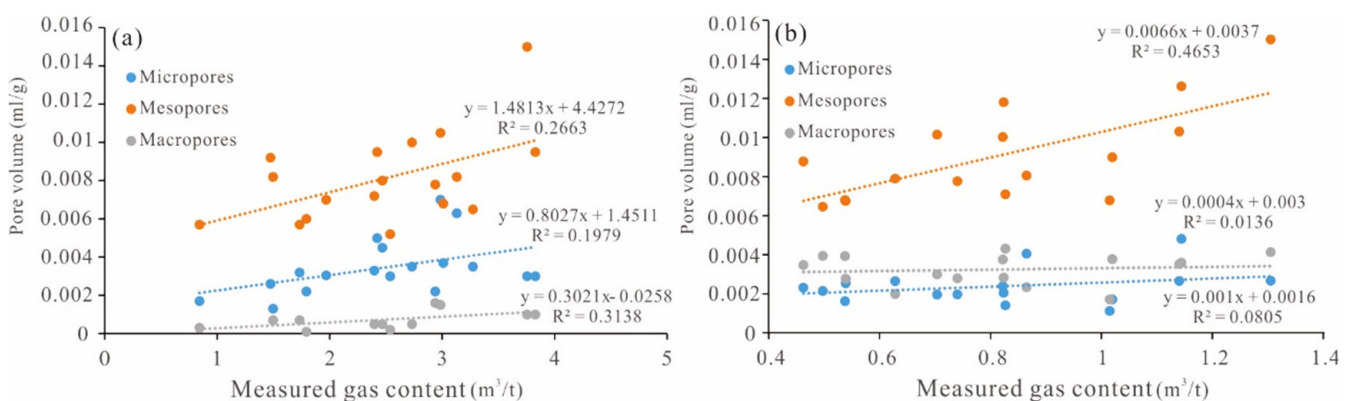

Figure 11. Effects of pore size on gas content in the Silurian Longmaxi marine shale (**a**) and Dongyuemiao lacustrine shale (**b**).

6. Conclusions

The S_1l organic-rich marine shale and the J_1d lacustrine shale in the Sichuan Basin, West China, are different in terms of pore type and pore structure. The former is dominated by organic pores, while the latter is primarily composed of clay-mineral pores, followed by organic pores. The pore system in the marine shale is mainly made up of micropores and mesopores with ink-bottle-like shapes, while in the lacustrine shale, it is mainly composed of mesopores and macropores with slit- or plate-like shapes.

Organic pores provide significant storage space for gas enrichment in both the S_1l organic-rich marine shale and the Dongyuemiao lacustrine shale. This also determines the adsorption capacity of the shale reservoirs, in which pores associated with water-swelling clay minerals contribute negatively to gas saturation. Although the S_1l marine shale and the J_1d shale reservoirs are different in terms of pore types, mesopores are the primary form of storage space in both, contributing significantly to shale-gas enrichment. Micropores are of secondary importance in the S_1l marine shale, while macropores are secondary contributors to pore volume in the J_1d lacustrine shale.

Data Availability Statement: No new data were created, or where data is unavailable due to privacy or ethical restrictions.

Conflicts of Interest: The authors declare no conflict of interest.

References

1. Wang, P.W.; Chen, Z.H.; Pang, X.Q. Revised models for determining TOC in shale play: Example from Devonian Duvernay Shale, Western Canada Sedimentary Basin. *Mar. Pet. Geol.* **2016**, *70*, 304–319. [CrossRef]
2. Ma, Y.S.; Cai, X.Y.; Zhao, P. China's shale gas exploration and development: Understanding and practice. *Pet. Explor. Dev.* **2018**, *45*, 589–603. [CrossRef]
3. Nie, H.K.; He, Z.L.; Wang, R.Y. Temperature and origin of fluid inclusions in shale veins of Wufeng–Longmaxi Formations, Sichuan Basin, South China: Implications for shale gas preservation and enrichment. *J. Pet. Sci. Eng.* **2020**, *193*, 107329. [CrossRef]
4. Nie, H.K.; Li, D.H.; Liu, G.X. An overview of the geology and production of the Fuling shale gas field, Sichuan Basin, China. *Energy Geosci.* **2020**, *1*, 147–164. [CrossRef]
5. Sun, C.X.; Nie, H.K.; Dang, W. Shale gas exploration and development in China: Current status, geological challenges and future directions. *Energy Fuels* **2021**, *35*, 6359–6379. [CrossRef]
6. Jiang, S.; Xu, Z.; Feng, Y. Geologic characteristics of hydrocarbon-bearing marine, transitional and lacustrine shales in China. *J. Asian Earth Sci.* **2016**, *115*, 404–418. [CrossRef]
7. Wang, P.W.; Liu, Z.B.; Chen, X. Impact of coexisted clay mineral and organic matter on pore growth in Lower Jurassic Da'anzhai lacustrine shale reservoir in the Northeast Sichuan Basin, West China. *Interpretation* **2021**, *9*, 1–53. [CrossRef]
8. Romero-Sarmiento, M.F.; Ducros, M.; Carpentier, B. Quantitative evaluation of TOC, organic porosity and gas retention distribution in a gas shale play using petroleum system modeling: Application to the Mississippian Barnett Shale. *Mar. Pet. Geol.* **2013**, *45*, 315–330. [CrossRef]
9. Dai, J.C.; Zou, S.; Liao, D. Geochemistry of the extremely high thermal maturity Longmaxi shale gas, southern Sichuan Basin. *Org. Geochem.* **2014**, *74*, 3–12. [CrossRef]
10. Shao, X.H.; Pang, X.Q.; Li, Q.W. Pore structure and fractal characteristics of organic-rich shales: A case study of the lower Silurian Longmaxi shales in the Sichuan Basin, SW China. *Mar. Pet. Geol.* **2017**, *80*, 192–202. [CrossRef]
11. Wang, P.F.; Jiang, Z.X.; Ji, W.M. Heterogeneity of intergranular, intraparticle and organic pores in Longmaxi shale in Sichuan Basin, South China: Evidence from SEM digital images and fractal and multifractal geometries. *Mar. Pet. Geol.* **2016**, *72*, 122–138. [CrossRef]
12. Clarkson, C.R.; Haghshenas, B.; Ghanizadeh, A. Nanopores to Megafractures: Current Challenges and Methods for Shale Gas Reservoir and Hydraulic Fracture Characterization. *J. Nat. Gas Sci. Eng.* **2016**, *31*, 612–657. [CrossRef]
13. Zhu, H.J.; Ju, Y.W.; Qi, Y. Impact of tectonism on pore type and pore structure evolution in organic-rich shale: Implications for gas storage and migration pathways in naturally deformed rocks. *Fuel* **2018**, *228*, 272–289. [CrossRef]
14. Gao, Z.Y.; Hu, Q.H. Pore structure and spontaneous imbibition characteristics of marine and continental shales in China. *AAPG Bull.* **2018**, *102*, 1941–1961. [CrossRef]

15. Wang, F.; Guo, S. Influential factors and model ofshale pore evolution: A case study of a continental shalefrom the Ordos Basin. *Mar. Pet. Geol.* **2019**, *102*, 271–282. [CrossRef]

16. Dong, T.; Harris, N.B.; McMillan, J.M. A model for porosity evo-lution in shale reservoirs: An example from the UpperDevonian Duvernay Formation, Western Canada Sedi-mentary Basin. *AAPG Bull.* **2019**, *103*, 1017–1044. [CrossRef]

17. Yang, C.J.; Zhang, X.; Tang, J. Comparative studyon micro-pore structure of marine, terrestrial, and transi-tional shales in key areas, China. *Int. J. Coal Geol.* **2017**, *171*, 76–92. [CrossRef]

18. Wu, S.; Yang, Z.; Zhai, X. An experimental study of organic matter, minerals andporosity evolution in shales within high-temperature and high-pressure constraints. *Mar. Pet. Geol.* **2019**, *102*, 377–390. [CrossRef]

19. Fathy, D.; Wagreich, M.; Sami, M. Geochemical evidence for photic zone euxinia during greenhouse climate in the Tethys Sea, Egypt. In *Advances in Geophysics, Tectonics and Petroleum Geosciences*; Springer: Cham, Switzerland, 2022; pp. 373–374.

20. Nie, H.K.; Jin, Z.J.; Sun, C.X. Organic matter types of the Wufeng and Longmaxi Formations in the Sichuan Basin, South China: Implications for the formation of organic matter pores. *Energy Fuels* **2019**, *33*, 8076–8100. [CrossRef]

21. Gao, Z.Y.; Xuan, Q.X.; Hu, Q.H. Pore structure evolution characteristics of continental shale in China as indicated from thermal simulation experiments. *AAPG Bull.* **2021**, *105*, 2159–2180. [CrossRef]

22. Liu, B.; Mastalerz, M.; Schieber, J. SEM petrography of dispersed organic matter in black shales: A review. *Earth-Sci. Rev.* **2022**, *224*, 103874. [CrossRef]

23. Ji, L.M.; Qiu, J.L.; Xia, Y.Q. Micro-pore characteristics and methane adsorption properties of common clay minerals by electron microscope scanning. *Acta Pet. Sin.* **2012**, *33*, 249–256.

24. Tang, X.; Zhang, J.C.; Jin, Z.J. Experimental investigation of thermal maturation on shale reservoir properties from hydrous pyrolysis of Chang 7 shale, Ordos Basin. *Mar. Pet. Geol.* **2015**, *64*, 165–172. [CrossRef]

25. Wood, D.A. Establishing credible reaction-kinetics distri-butions to fit and explain multi-heating rate S2 pyrolysispeaks of kerogens and shales. *Adv. Geo Energy Res.* **2019**, *3*, 1–28. [CrossRef]

26. Tian, H.; Pan, L.; Xiao, X.M. A preliminary study on the pore characterization of Lower Silurian black shales in the Chuandong Thrust Fold Belt, southwestern China using low pressure N2 adsorption and FE-SEM methods. *Mar. Pet. Geol.* **2013**, *48*, 8–19. [CrossRef]

27. Wang, Y.; Wang, L.H.; Wang, J.Q. Characterization of organic matter pores in typical marine and terrestrial shales, China. *J. Nat. Gas Sci. Eng.* **2017**, *49*, 56–65. [CrossRef]

28. Behar, F.; Vandenbroucke, M. Chemical modelling of kerogens. *Org. Geochem.* **1987**, *11*, 15–24. [CrossRef]

29. Li, P.; Hao, F.; Guo, X. Processes involved in the origin and accumulation of hydrocarbon gases in the Yuanba Gas Field, Sichuan Basin, Southwest China. *Mar. Pet. Geol.* **2015**, *59*, 150–165. [CrossRef]

30. Yang, R.; He, S.; Yi, J.Z. Nano-scale pore structure and fractal dimension of organic-rich wufeng-longmaxi shale from Jiaoshiba area, Sichuan Basin: Investigations using FE-SEM, gas adsorption and helium pycnometry. *Mar. Pet. Geol.* **2016**, *70*, 27–45. [CrossRef]

31. Nie, H.K.; Jin, Z.J.; Zhang, J.C. Characteristics of three organic matter pore types in the Wufeng-Longmaxi Shale of the Sichuan Basin, Southwest China. *Sci. Rep.* **2018**, *8*, 7014. [CrossRef]

32. Chen, L.; Lu, Y.; Jiang, S.; Li, J.; Guo, T.; Luo, C. Heterogeneity of the lower Silurian Longmaxi marine shale in the Southeast Sichuan Basin of China. *Mar. Pet. Geol.* **2015**, *65*, 232–246. [CrossRef]

33. Li, Y.J.; Feng, Y.Y.; Liu, H. Geological characteristics and resource potential of lacustrine shale gas in the Sichuan Basin, SW China. *Pet. Explor. Dev.* **2013**, *40*, 454–460. [CrossRef]

34. Gao, J.; Lin, L.B.; Ren, T.L. Controlling factors for shale gas enrichment of the Lower Jurassic Dongyuemiao member in the northern Sichuan Basin. *Lithol. Reserv.* **2016**, *28*, 67–75.

35. Zou, C.; Dong, D.; Wang, S. Geological characteristics and resource potential of shale gas in China. *Pet. Explor. Dev.* **2010**, *37*, 641–653. [CrossRef]

36. Ross, D.J.K.; Bustin, R.M. The importance of shale composition and pore structure upon gas storage potential of shale gas reservoirs. *Mar. Pet. Geol.* **2009**, *26*, 916–927. [CrossRef]

37. Zhang, T.; Ellis, G.S.; Ruppel, S.C. Effect of organic-matter type and thermal maturity on methane adsorption in shale-gas systems. *Org. Geochem.* **2012**, *47*, 120–131. [CrossRef]

38. Brunauer, S.; Emmett, P.H.; Teller, E.J. Adsorption of gases in multimolecular layers. *J. Am. Chem. Soc.* **1938**, *60*, 309–319. [CrossRef]

39. Langmuir, I. The adsorption of gases on plane surfaces of glass, mica and platinum. *J. Am. Chem. Soc.* **1918**, *40*, 1361–1403. [CrossRef]

40. Mosher, K.; He, J.; Liu, Y. Molecular simulation of methane adsorption in micro-and mesoporous carbons with applications to coal and gas shale systems. *Int. J. Coal Geol.* **2013**, *109*, 36–44. [CrossRef]

41. Cao, Z.; Jiang, H.; Zeng, J. Nanoscale liquid hydrocarbon adsorption on clay minerals: A molecular dynamics simulation of shale oils. *Chem. Eng. J.* **2020**, *420*, 127578. [CrossRef]

42. Wang, P.W.; Jin, Z.J.; Liu, G.X. Pore pressure prediction method for marine organic-rich shale: A case study of Wufeng-Longmaxi Shale in the Fuling Shale Gas Field, Northeast Sichuan Basin. *Oil. Gas Ind.* **2022**, *43*, 467–476.

43. Wang, P.W.; Chen, Z.H.; Hu, K.Z. The impact of organic pores on estimation ofoverpressure generated by gas generation in organic-rich shale: Example from Devonian Duvernay shale, Western Canada Sedimentary Basin. *AAPG Bull.* **2023**, *accepted*.

44. Ko, L.T.; Loucks, R.G.; Zhang, T. Pore and pore network evolution of upper cretaceous boquillas (Eagle ford-equivalent) mudrocks: Results from gold tube pyrolysis experiments. *AAPG Bull.* **2016**, *100*, 1693–1722. [CrossRef]

45. Ko, L.T.; Ruppel, S.C.; Loucks, R.G. Pore-types and pore-network evolution in Upper Devonian-Lower Mississippian Woodford and Mississippian Barnett mudstones: Insights from laboratory thermal maturation and organic petrology. *Int. J. Coal Geol.* **2018**, *190*, 3–28. [CrossRef]

46. Ardakani, O.H.; Sanei, H.; Ghanizadeh, A. Do all fractions of organic matter contribute equally in shale porosity? A case study from upper ordovician utica shale, southern quebec, canada. *Mar. Pet. Geol.* **2017**, *92*, 794–808. [CrossRef]

47. Rouquerol, J.; Avnir, D.; Fairbridge, C. Recommendations for the characterization of porous solids (Technical Report). *Pure Appl. Chem.* **1994**, *66*, 1739–1758. [CrossRef]

48. Liu, W.P.; Zhang, C.L.; Gao, G.D. Controlling factors and evolution laws of shale porosity in Longmaxi Formation, Sichuan Basin. *Acta Pet. Sin.* **2017**, *38*, 175–184.

49. Gregg, S.; Sing, K. *Adsorption, Surface Area and Porosity*, 2nd ed.; Academic Press: London, UK, 1982.

50. Sing, K.S. Reporting physisorption data for gas/solid systems with special reference to the determination of surface area and porosity. *Pure Appl. Chem.* **1985**, *57*, 603–619. [CrossRef]

51. Hickey, J.J.; Bo, H. Lithofacies summary of the Mississippian Barnett Shale, Mitchell 2 T.P. Sims well, Wise County, Texas. *AAPG Bull.* **2007**, *91*, 437–443. [CrossRef]

52. Chalmers, G.R.L.; Bustin, R.M. The organic matter distribution and methane capacity of the lower cretaceous strata of northeastern British Columbia, Canada. *Int. J. Coal Geol.* **2007**, *70*, 223–239. [CrossRef]

53. Li, J.; Li, X.F.; Wang, X.Z. Effect of water distribution on methane adsorption capacity of shale clay. *Chin. J. Theor. Appl. Mech.* **2016**, *5*, 1217–1228. [CrossRef]

54. Ji, L.M.; Zhang, T.; Milliken, K. Experimental investigation of main controls to methane adsorption in clay-rich rocks. *Appl. Geochem.* **2012**, *27*, 2533–2545. [CrossRef]

55. Lu, X.C.; Li, F.C.; Watson, A.T. Adsorption Measurements in Devonian Shales. *Fuel* **1995**, *74*, 599–603. [CrossRef]